




## Overcoming strength-toughness trade-off in a eutectic high entropy alloy by optimizing chemical and microstructural heterogeneities

Zhaoqi Chen<sup>1,6</sup>, Wenqing Zhu <sup>1,6</sup>, Hang Wang<sup>1</sup>, Quanfeng He<sup>1,2</sup>, Qihong Fang<sup>3</sup>, Xiaodi Liu<sup>4</sup>, Jia Li <sup>3</sup>✉ & Yong Yang <sup>1,5</sup>✉

The well-known strength-toughness trade-off has long been an obstacle in the pursuit of advanced structural alloys. Here, we develop a eutectic high entropy alloy that effectively overcomes this limitation. Our alloy is composed of face-centered cubic and body-centered cubic crystalline phases, and demonstrates attractive mechanical properties by harnessing microstructural hybridization and a strain-induced phase transition between phases. Unlike conventional eutectic alloys, the compositionally complexity of our alloy allows control of its microstructural and chemical heterogeneities across multiple length scales, ranging from atomic- and nano-scales to meso-scales. Optimizing these microstructural and chemical heterogeneities within our alloy enables high strength and ductility because of enhanced fracture resistance, outperforming alternative high and medium entropy alloys with similar compositions and microstructures.

<sup>1</sup>Department of Mechanical Engineering, City University of Hong Kong, Kowloon Tong, Kowloon, Hong Kong 999077, China. <sup>2</sup>Institute of Materials Modification and Modelling, School of Materials Science and Engineering, Shanghai Jiao Tong University, Shanghai 200240, China. <sup>3</sup>State Key Laboratory of Advanced Design and Manufacturing for Vehicle Body, College of Mechanical and Vehicle Engineering, Hunan University, Changsha 410082, China. <sup>4</sup>College of Mechatronics and Control Engineering, Shenzhen University, Shenzhen 518060, China. <sup>5</sup>Department of Materials Science and Engineering, City University of Hong Kong, Kowloon Tong, Kowloon 999077, China. <sup>6</sup>These authors contributed equally: Zhaoqi Chen, Wenqing Zhu. ✉email: [lijia123@hnu.edu.cn](mailto:lijia123@hnu.edu.cn); [yonyang@cityu.edu.hk](mailto:yonyang@cityu.edu.hk)

Eutectic alloys have been important in engineering applications due to their high rupture strength<sup>1</sup>, good creep resistance<sup>2</sup> and excellent castability<sup>3</sup>. The microstructure, consisting of two or more phases forming in a coupled manner, enables superior mechanical properties compared to single-phased alloys. Extensive research over the years has been conducted to develop a variety of eutectic systems, including Al-Si<sup>4</sup>, NiAl-Mo<sup>5</sup> and Al-Fe-Nb<sup>6</sup>. However, only a few eutectic systems are commercially significant, as many others have shown unsatisfactory deformability and limited toughening mechanism<sup>7,8</sup>. High entropy alloys (HEAs)<sup>9,10</sup> represent a break-through in conventional alloys design, providing rich opportunities for the discovery of eutectic alloys in an expanded compositional space. Lu et al.<sup>11</sup> first proposed the concept of eutectic high entropy alloys (EHEAs), which combine the advantages of both eutectic alloys and HEAs with good castability and a balanced strength-ductility combination<sup>12,13</sup>. As a result, EHEAs have gained tremendous research interest in recent decades<sup>3,14–21</sup>.

To optimize the mechanical properties of EHEAs, thermomechanical processing is crucial for tailoring microstructure heterogeneity through deformation and subsequent heat treatments<sup>22,23</sup>. Although various strengthening mechanisms, such as precipitation strengthening<sup>24</sup> and grain refinement strengthening<sup>25</sup>, have been successfully achieved in EHEAs after thermomechanical processing, they often come at the expense of toughness and/or ductility due to strain localization and premature fracture caused by precipitation or grain boundaries. In EHEAs, the interfaces of soft and hard phases can lead to heterogeneous deformation-induced (HDI) strengthening, but they are also the preferable sites for crack nucleation and propagation<sup>26</sup>, which can result in premature failure of EHEAs. Therefore, achieving both strengthening and toughening simultaneously through tailoring the microstructure heterogeneity in EHEAs remains a challenge.

In this study, we developed a EHEA with the chemical composition of Al<sub>18</sub>Co<sub>30</sub>Cr<sub>11</sub>Fe<sub>11</sub>Ni<sub>30</sub> (in atomic percentage), which exhibits a balanced strength-ductility combination surpassing those of previously reported Al-Co-Cr-Fe-Ni alloys, including EHEAs<sup>13,27</sup>, single-phased and dual-phased HEAs<sup>28–30</sup>. We employed a thermomechanical processing method to systematically tune the chemical and microstructural heterogeneity of the alloy at various levels. Our EHEA demonstrated deformation-induced phase transformation, a mechanism for enhancing plasticity strengthening that is rarely observed in other EHEAs. Furthermore, we discovered that by adjusting the morphological heterogeneity of the eutectic microstructure in our alloy, we can achieve significant toughening by delocalizing micro-cracks at the hard/softer interface, effectively mitigating local stress concentration even at high flow stress and hence enhancing the overall ductility of our EHEA.

## Results

**Microstructural characterization of the Al<sub>18</sub>Co<sub>30</sub>Cr<sub>11</sub>Fe<sub>11</sub>Ni<sub>30</sub> EHEA.** The as-cast (AC) Al<sub>18</sub>Co<sub>30</sub>Cr<sub>11</sub>Fe<sub>11</sub>Ni<sub>30</sub> EHEA is shown to have a dual-phase structure in Fig. 1a, as evidenced by the presence of two sets of peaks corresponding to the face-centered cubic (FCC) and body-centered cubic (BCC) phase. Electron back-scattering diffraction (EBSD) analysis further confirms the dual-phase structure, revealing a eutectic lamellar morphology with lamellae thickness of  $1.18 \pm 0.53 \mu\text{m}$  and  $0.51 \pm 0.33 \mu\text{m}$  for the FCC and BCC phase, respectively (Fig. 1a, Supplementary Fig. 1a). The FCC phase is found to maintain a Kurdjumov–Sachs (K–S) ( $\{111\}_{\text{FCC}}//\{110\}_{\text{BCC}}$ ,  $\langle 110 \rangle_{\text{FCC}}//\langle 111 \rangle_{\text{BCC}}$ ) orientation relationship with the adjacent BCC phase in the AC state, which is also revealed by the grain boundary map (the inset of Fig. 1a)

and is consistent with the observations in a few (FCC + BCC) dual-phase HEAs<sup>31,32</sup>. The alternating dual-phase lamellar structure of the Al<sub>18</sub>Co<sub>30</sub>Cr<sub>11</sub>Fe<sub>11</sub>Ni<sub>30</sub> EHEA is clearly shown in the transmission electron microscopy (TEM) image (Fig. 1b). Additionally, several misfit dislocations are observed at the interface between the FCC and BCC phase, indicating semi-coherent interfaces. The Fast Fourier Transform images confirm the presence of the K–S orientation relationship between the FCC and BCC phase (Fig. 1c–f). The energy-dispersive spectroscopy (EDS) maps reveal that the FCC phase is rich in Co, Cr, and Fe, while the BCC phase is rich in Al and Ni (Fig. 1g).

To tailor the microstructure heterogeneity of the EHEA, we conducted cold rolling and annealing treatments and labeled the resulting cold-rolled, annealed EHEAs at 700 °C, 800 °C and 900 °C as CR, P1, P2, and P3, respectively. Following thermo-mechanical processing, we observed that the EHEAs still contained both FCC and BCC phases, which are illustrated in Fig. 2a by the absence of new phase peaks. EDX analyses were conducted to assess the evolution of chemical concentration in the EHEA with only Al and Cr displayed in Fig. 2b as the representatives of the chemical change in the BCC- and FCC-phases. We found significant changes in chemical concentration after the annealing treatments, with the FCC phase exhibiting a higher concentration of Co, Cr, Fe and a lower concentration of Al, Ni compared to that in the AC and CR EHEAs (see Supplementary Fig. 2 for the comprehensive results). Conversely, the BCC phase exhibited the opposite results. We have employed the Thermo-Calc software to calculate the equilibrium phase diagrams, as depicted in Supplementary Fig. 3. Remarkably, these calculated diagrams align with our experimental results, indicating that the annealing process induces further chemical diffusion, resulting in higher concentrations of Co, Cr and Fe within the FCC phase and a higher concentration of Al within the BCC phase. During annealing treatments, recrystallization occurred and gradually replaced the lamellar structure with a near-equiaxed one and significantly decreased lamellae thickness, as observed in Fig. 2c and Supplementary Fig. 1a. Notably, the recrystallization process is more pronounced in the FCC phase than that in the BCC phase, probably due to strain partitioning during cold deformation<sup>26</sup>, as evidenced by the higher fraction of near-equiaxed structures in the FCC phase (Supplementary Fig. 1b). In addition, the grain boundary maps of the annealed EHEAs are shown in Fig. 2d. In the P1 EHEA, some low angle grain boundaries (LAGBs) are still preserved indicative of incomplete recrystallization. Furthermore, the statistical result shows that after cold rolling, most interfaces deviate from the K–S relationship, which is also observed in other alloys<sup>33,34</sup> and usually attributed to crystal rotation during severe plastic deformation. It is noteworthy that the fraction of the K–S relationship increases after the annealing treatments (Fig. 1d), indicating the restoration of the K–S orientation relationship at the FCC/BCC interfaces. Considering the limited field of view in Fig. 1a and Fig. 2c, d, we have included the EBSD results at a lower magnification in Supplementary Fig. 4, which exhibit good consistency with the high-magnification results, indicating that the observed microstructural evolution is representative of the overall microstructure.

## Mechanical properties of the Al<sub>18</sub>Co<sub>30</sub>Cr<sub>11</sub>Fe<sub>11</sub>Ni<sub>30</sub> EHEA.

Figure 3a illustrates the true stress-strain curves obtained from testing our EHEAs before and after undergoing thermomechanical treatments (see Methods for details; the corresponding engineering stress-strain curves are provided in Supplementary Fig. 6). In our current study, we conducted numerous tensile tests on samples obtained under various

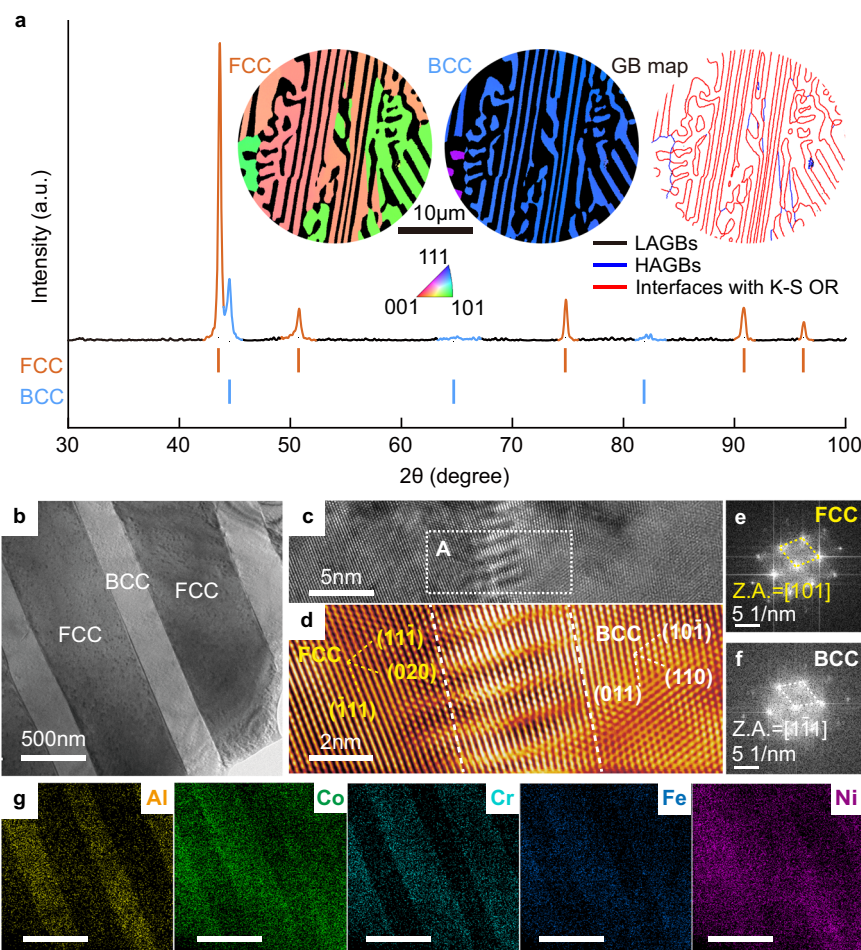


**Fig. 1** The structural characterization of the as-cast  $\text{Al}_{18}\text{Co}_{30}\text{Cr}_{11}\text{Fe}_{11}\text{Ni}_{30}$  eutectic high entropy alloy. **a** The XRD pattern of the as-cast EHEA that comprises an FCC and a BCC phase. The insets show the inverse pole figures (IPFs) of the FCC and BCC phase with a lamellar microstructure. The grain boundary map shows low-angle grain boundaries (colored in black) with misorientations  $2^\circ \leq \theta \leq 15^\circ$ , high-angle grain boundaries (in blue) with  $\theta > 15^\circ$  and FCC/BCC interfaces with the K-S orientation relationship (in red). **b** The TEM bright field image of the dual-phase lamellar structure. **c** The high resolution transmission electron microscopy (HRTEM) image showing the FCC/BCC interface. **d** The Fast Fourier Transform (FFT) filtered image of the region A in (**c**) which reveals misfit dislocations at the semi-coherent FCC/BCC. **e-f** The FFT patterns of the FCC and BCC phase that shows the K-S orientation relationship. **g** The elemental mappings of the lamellar microstructure are shown in (**b**). Scale bar = 500 nm.

thermomechanical treatment conditions. Supplementary Fig. 7 showcases the stress-strain curves obtained from the AC EHEA. Given that the presence of casting defects often leads to mechanical property variations in alloys<sup>35,36</sup>, the remarkable repeatability of our results suggests that any potential influence of casting defects in our AC samples can be considered negligible. Furthermore, we conducted 3D X-ray Computed Tomography (CT) scanning on our as-cast sample, with imaging performed at a resolution of 10  $\mu\text{m}$  (see Methods). Notably, the CT imaging did not reveal the presence of any significant casting defects (see Supplementary Fig. 8), further supporting our conclusion derived from the tensile tests. The AC EHEA showed a yield strength of  $618 \pm 14$  MPa and a uniform elongation of  $8.6 \pm 0.6\%$  before fracture. After cold rolling, the yield strength of the CR EHEA increased to  $\sim 1800$  MPa with a concomitant reduction in ductility to  $\sim 2\%$ . Subsequent thermal annealing at 700  $^\circ\text{C}$  and 800  $^\circ\text{C}$  led to a decrease in strength and an increase in ductility, which is anticipated due to annealing induced recrystallization and microstructural coarsening<sup>37,38</sup>, as seen in Fig. 2c. However, thermal annealing at temperature of 900  $^\circ\text{C}$  and above (see Method) triggered a rather swift degradation of both the strength and the ductility of our EHEAs. By comparison, our P2 EHEAs exhibited the most desirable combination of strength and

ductility, registering  $1041 \pm 33$  MPa and  $17.0 \pm 0.6\%$ , respectively. In other words, compared with the AC EHEA, our study revealed that proper thermal annealing achieved up to twofold improvement in ductility and 70% strength gain.

In Fig. 3b, the strain hardening rate curves for the EHEAs are depicted. Specifically, the strain hardening of the annealed EHEAs can be distinguished by a three-stage process. Stage A signifies the initial reduction in the strain hardening rate ( $\theta$ ), followed by Stage B, where the strain hardening rate starts increasing after a true strain of 1.3%, reminiscent of dynamic hardening caused by deformation twinning<sup>23,39,40</sup>. The process culminates in Stage C, where  $\theta$  exhibits a gradual decline until failure (fracture). On the other hand, the AC and CR EHEAs demonstrate two-stage hardening without Stage B. It is noteworthy that none of the EHEAs satisfies the Considerer's instability criterion<sup>41,42</sup>, indicating that necking is not the prevalent fracture mechanism as has been reported in previous studies<sup>43–45</sup>. Figure 3c displays the micrographs of the fractured AC and P2 EHEAs. The P2 EHEA surface displays numerous microcracks proximate to the fracture plane, while no microcrack is seen in the AC EHEA. The fracture surfaces of both EHEAs exhibit ductile fracture morphology characterized by dimples, indicating a similar fracture mechanism. Figure 3d compares our

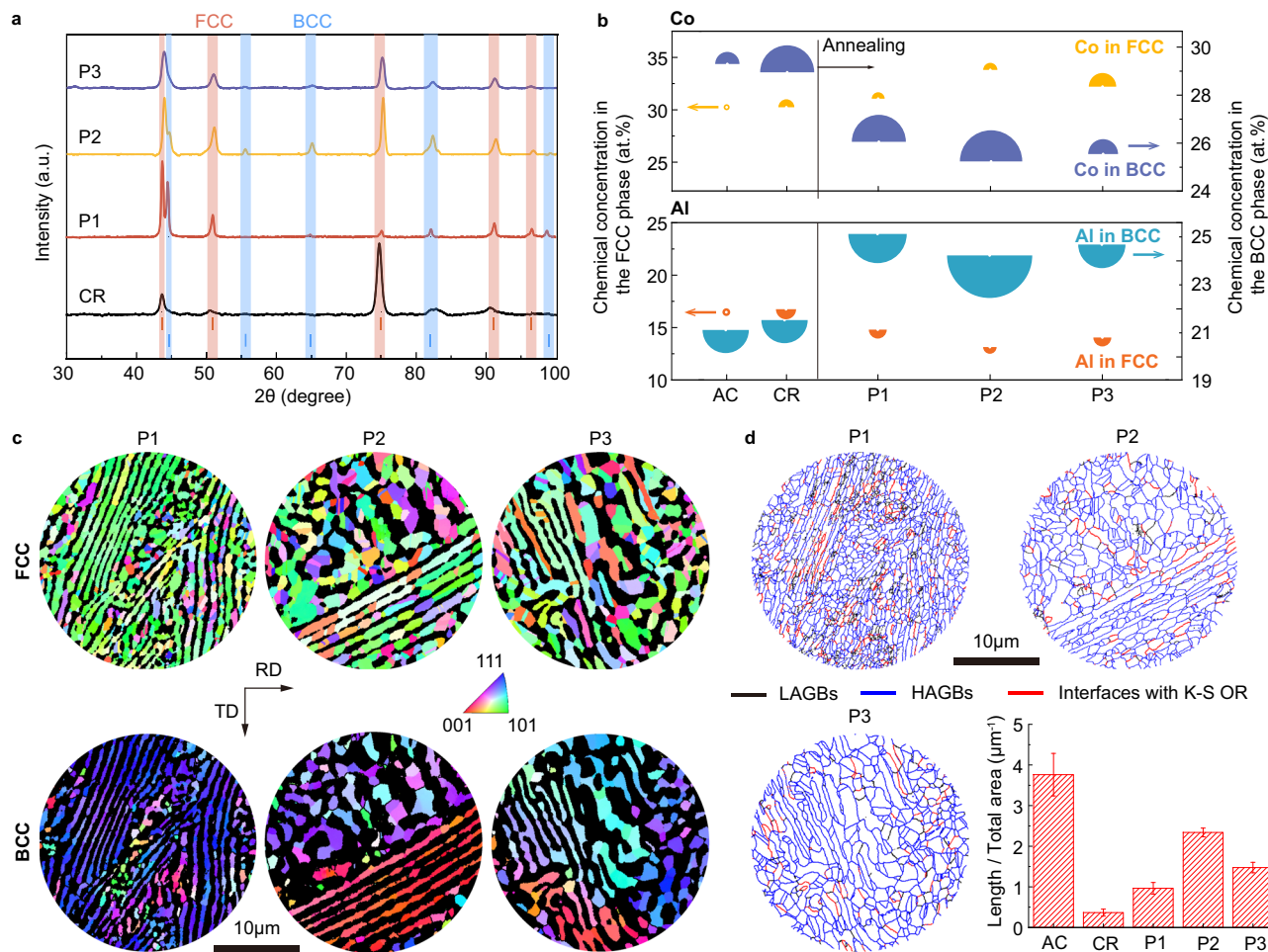


**Fig. 2** The structural characterization of the  $\text{Al}_{18}\text{Co}_{30}\text{Cr}_{11}\text{Fe}_{11}\text{Ni}_{30}$  eutectic high entropy alloy after thermomechanical treatments. **a** The XRD patterns of the cold-rolled and annealed EHEAs comprising the FCC and BCC phase. **b** The chemical concentrations of Al and Co elements in the lamellar structure of the EHEAs. The center and radius of the semicircles represent the average and standard deviation of concentrations. **c** The inverse pole figures of the FCC and BCC phase in a lamellar and/or near-equiaxed microstructure. **d** The grain boundary maps highlighting the FCC/BCC interfaces with the K-S orientation relationship displayed in red. The statistical result of the length of the interfaces with the K-S orientation relationship (measured in  $\mu\text{m}$ ) over the total detection area (measured in  $\mu\text{m}^2$ ) in the annealed EHEAs. The IPF maps and grain boundary maps of the CR EHEAs are shown in Supplementary Fig. 5.

EHEAs to single-, multi-phased HEAs and EHEAs in the Al-Co-Cr-Fe-Ni family with regard to their strength and ductility (see Supplementary Table 1 for details). While thermomechanical processing of conventional metals leads to the trade-off between strength and ductility<sup>37,38,46</sup>, however, it is clear that our P2 EHEA is breaking this norm by delivering exceptional strength-ductility combination when compared to other HEAs and EHEAs. Notably, further annealing led to degradation of both strength and ductility. This finding is intriguing and merits further in-depth analyses.

**Microstructural evolution during deformation.** Figure 4a presents a detailed visual representation of the microstructures observed in our EHEA samples (specifically, the AC and P2 samples) after tensile deformation. In the AC sample, dislocation-mediated plasticity was observed within its eutectic structure, with the proportions of FCC and BCC phases remaining unchanged after deformation. In contrast, Fig. 4b demonstrates a significant strain-induced transformation from FCC to BCC in the annealed EHEAs. It is widely accepted that the propensity of strain-induced phase transformation increases as the stacking

fault energy (SFE) of an alloy decreases. It is noteworthy that Al in the Al-Co-Cr-Fe-Ni system possesses the highest SFE<sup>47</sup>. Hence, we anticipate that there could be other compositions within the EHEA system, featuring lower Al concentrations could demonstrate remarkable plasticity due to deformation-induced FCC-BCC transitions. Figure 4c depicts further examination of an annealed EHEA after tensile deformation, revealing the emission of a stacking fault at the FCC/BCC interface with a K-S orientation relationship (see the inset in Fig. 4c). Adjacent to the stacking fault, a Shockley partial dislocation (i.e.,  $1/6[112]$ ) was identified using the dislocation circuit (Fig. 4d and the inset). A notable observation was the change in atomic packing across the FCC/BCC interface, characterized by measuring the angles ( $\alpha$  and  $\beta$ ) between atomic planes, as shown in Fig. 4e. It was found that from Region A to B and C, the ( $\alpha$ ,  $\beta$ ) angle gradually changed from ( $71.9^\circ \pm 1.3^\circ$ ,  $125.6^\circ \pm 0.9^\circ$ ) to ( $66.9^\circ \pm 1.3^\circ$ ,  $122.3^\circ \pm 1.2^\circ$ ) and finally to ( $59.7^\circ \pm 1.5^\circ$ ,  $119.8^\circ \pm 0.9^\circ$ ) (Fig. 4f, g). In comparison, a standard crystal lattice maintains ( $\alpha$ ,  $\beta$ ) values of ( $70.5^\circ$ ,  $125.3^\circ$ ) for an FCC lattice, when viewed along the  $\langle 110 \rangle$  direction, and ( $60^\circ$ ,  $120^\circ$ ) for a BCC lattice viewed along the  $\langle 111 \rangle$  direction. Therefore, the variation of measured angles can be considered an early indication for the FCC to BCC transition in

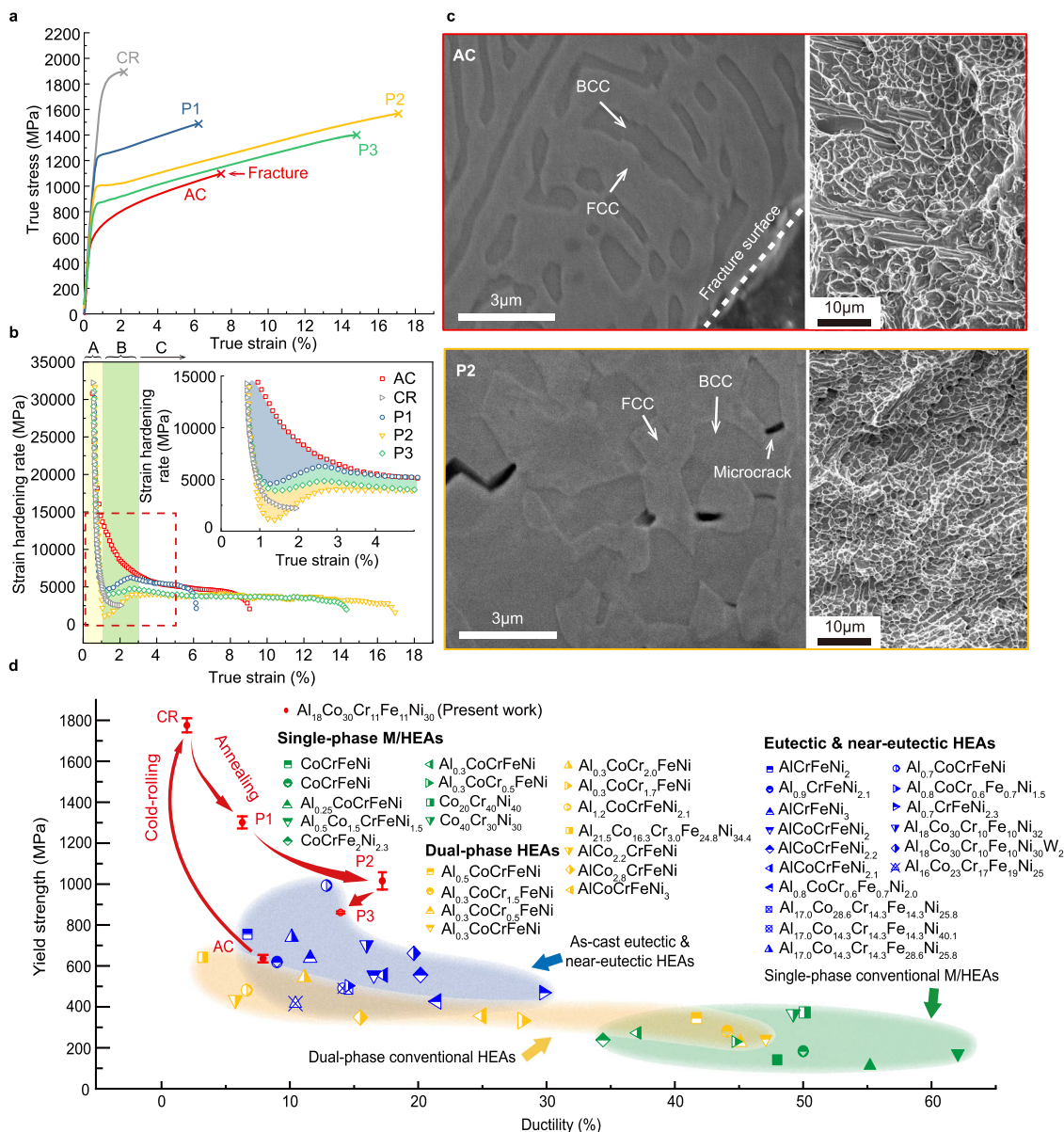


**Fig. 3** The mechanical characterization of the  $\text{Al}_{18}\text{Co}_{30}\text{Cr}_{11}\text{Fe}_{11}\text{Ni}_{30}$  eutectic high entropy alloy. **a** The typical uniaxial true stress-strain curves of our EHEAs. **b** The curves of strain hardening rate versus strain for the EHEAs. The inset shows the enlarged region marked by the red rectangular. **c** The fracture morphologies observed on the AC and P2 EHEA samples (left panel: the plan view of the sample surface next to the fractured surface; right panel: the plan view of the fracture surfaces). **d** Comparison of our  $\text{Al}_{18}\text{Co}_{30}\text{Cr}_{11}\text{Fe}_{11}\text{Ni}_{30}$  EHEAs to single-phased, dual-phased M/HEAs and EHEAs in the Al-Co-Cr-Fe-Ni family with regards to their strength and ductility.

Region B, following the emission of the partial dislocation and the formation of the stacking fault. Furthermore, our analysis reveals that there is no presence of an ordered phase in the AC and P2 EHEAs, both before and after deformation. This finding indicates that the observed dynamic strain hardening is not attributed to an order-disorder transition, as depicted in Fig. 1 and Supplementary Fig. 9.

## Discussion

To understand the mechanisms behind the deformation-induced phase transformation, we conducted extensive molecular dynamics (MD) simulations on the shear deformation in our dual-phase HEAs (see Methods). To accurately represent real-world observations, we constructed “sandwich-like” simulation cells consisting of three layers of phases (e.g., BCC/FCC/BCC), with the chemical

composition of each phase assigned based on the results obtained from the annealed or as-cast samples (e.g., P2 or AC EHEA). The FCC/BCC interfaces maintained the K-S orientation relationship, regardless of the chemical compositions of different phases (Supplementary Fig. 10). Figure 5a displays the snapshots of the simulated FCC-BCC phase transformation process in the model P2 EHEA. Interestingly, local BCC-like atomic packings could be identified in the FCC phase prior to deformation, which could be attributed to the effect of lattice distortion<sup>48,49</sup>. However, while the regions of local BCC-like packing increased with shear strain, phase transformation began at the initial FCC/BCC interfaces and gradually propagated into the FCC phase until the complete phase transformation occurred. Figure 5b–e shows the trajectories of atoms at the interface during the phase transformation. Notably, the migration of the FCC/BCC interface occurred in two steps. Initially, atoms in the FCC phase collectively moved along the

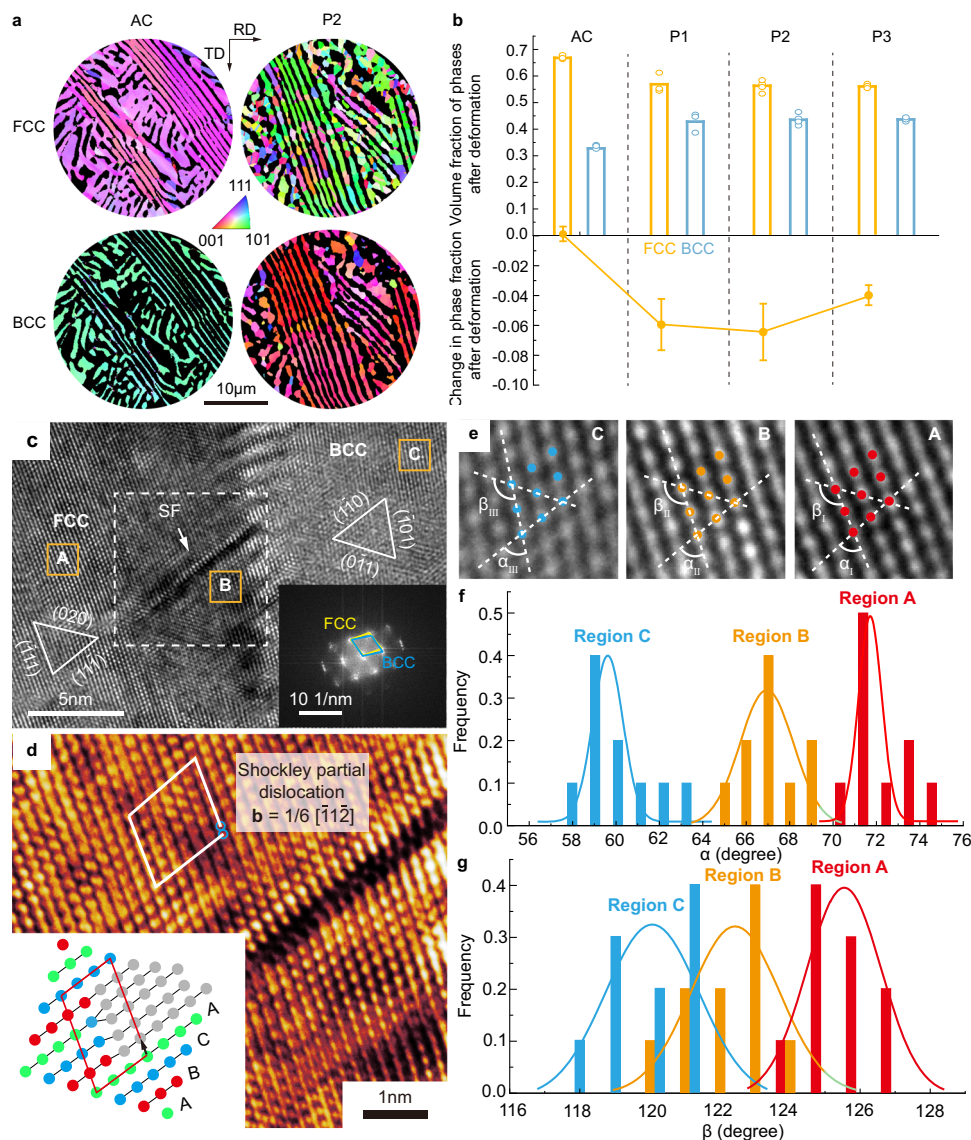


**Fig. 4** The microstructure characterization of the deformed  $\text{Al}_{18}\text{Co}_{30}\text{Cr}_{11}\text{Fe}_{11}\text{Ni}_{30}$  eutectic high entropy alloy. **a** The inverse pole figures of the FCC and BCC phase in the deformed AC and P2 EHEAs. **b** Volume fraction of the FCC and BCC phase and the fraction changes of the FCC phase after tensile deformation in the EHEAs. **c** High-resolution transmission electron microscopy (HRTEM) images of the deformed P2 EHEA. The inset shows the corresponding Fast Fourier transformation (FFT) pattern. **d** Enlarged view of the white dotted rectangular area in **c**. The inset is a schematic diagram of the stacking fault. **e** Enlarged HRTEM images of region A, B, and C in **(c)**. **f, g** The distribution of the measured angle of  $\alpha$ ,  $\beta$ , respectively.

$[\bar{1}\bar{1}\bar{1}]$  direction causing a change in the bond angle of the otherwise perfect  $(\bar{1}\bar{1}0)_{\text{FCC}}$  lattice from  $90^\circ$  to approximately  $84^\circ$ , as observed in Fig. 5b–e. Subsequently, atom displacement shifted towards the  $[\bar{1}\bar{1}\bar{2}]$  direction leading to the formation a BCC lattice. This resulted in the transformation of the initial  $(\bar{1}\bar{1}0)_{\text{FCC}}$  plane into a  $(\bar{1}\bar{1}\bar{1})_{\text{BCC}}$  plane, as schematically illustrated in Fig. 5f. The two-step-shear mechanism is in line with the crystallographic theory, which postulates that the phase transformation from FCC to BCC involves two distinct shear deformations within the interface region<sup>50</sup>. It is noteworthy that the transformed BCC lattice maintained the same atomic configuration as the initial BCC lattice (Fig. 5e), thereby retaining the K-S orientation relationship<sup>51</sup>.

To investigate the cause of the unusual paths taken by atom (Fig. 5f), we conducted a detailed analysis of the motion of defects accompanying the phase transformation. By examining the atomic packing near the FCC/BCC interface (Fig. 5g), we were able to identify partial dislocations using the well-established dislocation extraction algorithm<sup>52</sup>, as illustrated in Fig. 5h.

Importantly, these partial dislocations move away from the FCC/BCC interface into the FCC phase through gliding (See Supplementary Movie 1), leading to the formation of local BCC lattices within the FCC phase. Consequently, the atomic trajectories observed earlier (Fig. 5i) were a direct result of these passing dislocations, as they left behind a trail of transformed regions. Hence, in our P2 EHEA, the transformation pathway involves the two-step shear deformation through gliding of partial dislocations.

For the strain-induced FCC-BCC phase transformation, orientation relationships play a crucial role in adjusting the FCC/BCC interfacial energy and controlling dislocation behavior<sup>53,54</sup>. It has been revealed that the selection of different orientation relationships can significantly influence the transformation process in MD simulations<sup>55</sup>. To assess the importance of the K-S relationship in our EHEA, we extended our investigations through additional MD simulations where we deliberately introduced variation in the orientation relationship or chemical

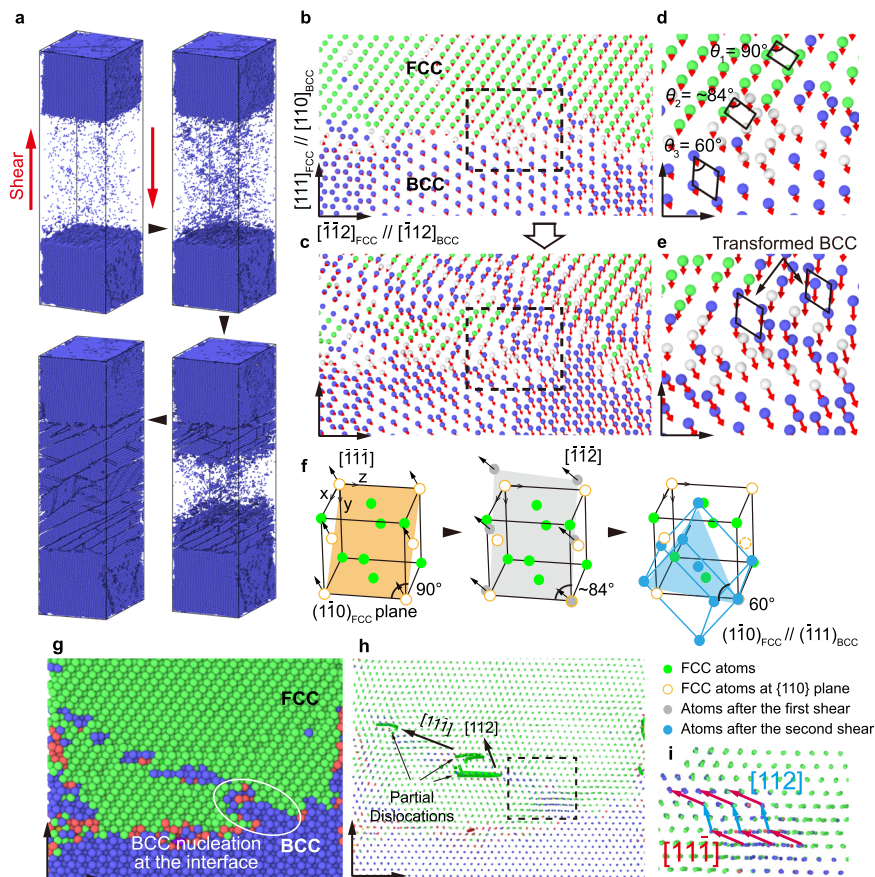


**Fig. 5** The molecular dynamics simulation results revealing phase transformation mechanism of the  $\text{Al}_{18}\text{Co}_{30}\text{Cr}_{11}\text{Fe}_{11}\text{Ni}_{30}$  eutectic high entropy alloy.

**a** Snapshots of the calculation cell showing the FCC-BCC transformation process with the K-S orientation relationship. Only atoms with BCC configuration are shown. **b-c** Cross-sectional view of the FCC/BCC interface with 3D displacement vectors. Colors denote the local crystal structure. **d-e** Enlarged view of the black dotted rectangular area in (**b**, **c**), respectively. **f** Schematic representation of the FCC  $\rightarrow$  BCC phase transformation mechanism. **g** Cross-sectional view showing the nucleation of the BCC phase at the FCC/BCC interface and (**h**) the extracted dislocation lines ahead of transition region for the two-step-shear transformation mechanism. **i** Enlarge view of the black dotted rectangular area in (**h**).

compositions at the FCC/BCC interface, deviating from our P2 EHEA. Supplementary Fig. 11a, b illustrate the outcomes of the simulations. Notably, when we remove the BCC phase in the simulation cell, we only observed the formation of stacking faults without any occurrence of FCC-BCC transformation in the remaining FCC single crystals. Furthermore, modifying the chemical compositions of the phases led to an increase in the interfacial energy between the FCC and BCC phases, even when a K-S orientation relationship was maintained (Supplementary Fig. 11c). According to the classical nucleation model<sup>56,57</sup>, a higher interfacial energy corresponds to a larger nucleation barrier, effectively suppressing phase transformation. Furthermore, Supplementary Fig. 12 presents the cross-sectional view of the near-interface FCC phase along the  $\bar{1}\bar{1}2_{\text{FCC}}//[\bar{1}12]$  direction. Notably, in the AC EHEA, stacking faults align in the same direction. However, in the P2 annealed EHEA, an increased number of stacking faults are emitted along different direction, intersecting with each other, which is consistent with the experimental observations (see Supplementary Fig. 12c). This arrangement of stacking faults generates local stress field, enabling the FCC lattice to exceed the critical stress threshold and undergo a transform to the BCC lattice<sup>58</sup>, leading to the dynamic hardening effect in the annealed EHEAs. These findings rationalize our experimental observations that plasticity occurred in our AC EHEA mainly by dislocation mechanisms but in our annealed EHEAs by combined dislocation and phase transition mechanisms.

In addition to phase transition, the microstructure of our EHEA also plays a significant role for enhanced ductility and the formation of abundant micro-cracks (Fig. 3c and Supplementary Fig. 13). These micro-cracks can enhance the toughness of our EHEA by increasing energy dissipation before catastrophic failure occurs. To investigate this microstructure effect, we conducted extensive finite element (FE) simulations (see Methods) that combined dislocation-based crystal plasticity<sup>59</sup> with phase-field modeling<sup>60</sup>. These simulations considered damages caused by excessive dislocation accumulation, and further details can be found in Supplementary Note 1, 2. We created three pre-cracked microstructure models using phase-field techniques<sup>61,62</sup>, which simulated solidification into lamellar (model 1), mixed (model 2) and equiaxed (model 3) microstructures (see Supplementary Fig. 14, Supplementary Note 1, Supplementary Table 2, 3, Fig. 6a-c). Due to the structural anisotropy present in model 1, we analyzed cracking parallel (model 1-h) and perpendicular (model 1-v) to the lamellas in this model. On the other hand, model 2 and 3 exhibited limited structural anisotropy, resulting in fracture resistance that was insensitive to cracking direction. Subsequently, we applied tensile loading to all models until overall failure was detected (Fig. 6d).

The results indicated that cracking in model 2 or along the direction perpendicular to lamellas in model 1 was the most challenging and exhibited distributed local damages ahead of the main crack-tip (Fig. 6e-h). In comparison, damages were concentrated at the main crack-tip in model 3 or in model 1 when the

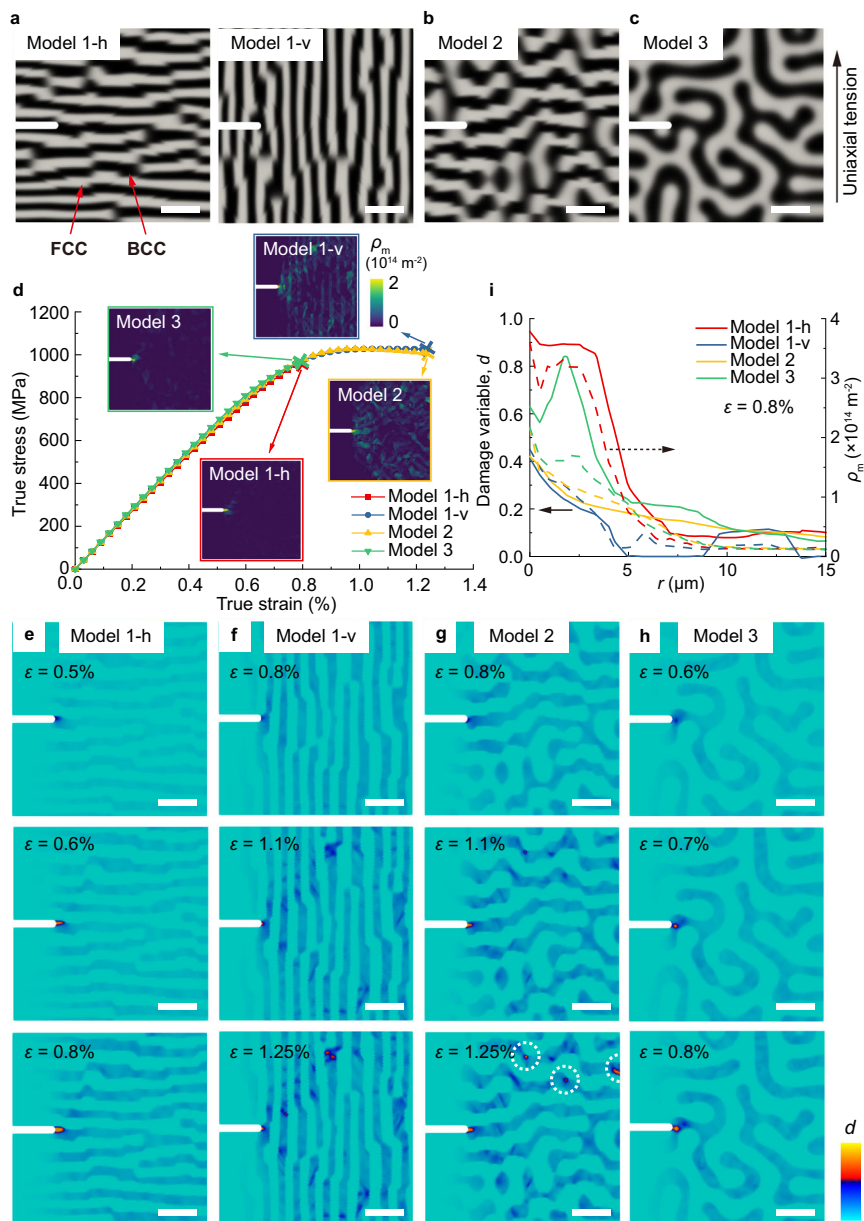


**Fig. 6** Crystal plasticity simulation results revealing the microstructural effect on the fracture behavior of the  $\text{Al}_{18}\text{Co}_{30}\text{Cr}_{11}\text{Fe}_{11}\text{Ni}_{30}$  eutectic high entropy alloy. **a–c** Computational models generated by the phase-field model. **d** Stress-strain curves of the four models. Insets are the contours of the mobile dislocation density  $\rho_m$  at the failure points. **e–h** Snapshots of the fields of damage variable  $d$  of the four models. **i** Profiles of  $d$  and  $\rho_m$  at strain of 0.8% along the pre-set crack ( $r = 0$  corresponds to the crack tip). Scale bar = 20  $\mu\text{m}$ .

crack was oriented along the direction parallel to lamellas. These findings have significant implications: (1) the fracture resistance of the lamellar microstructure is directionally dependent, with cracking preferentially occurring in directions parallel to local FCC/BCC interfaces in the AC EHEA<sup>21</sup>. This observation aligns with the “furrow” like features observed on the fracture surface in our experiments (see Fig. 3c and Supplementary Fig. 13). (2) The fracture resistance of the equiaxed microstructure is weak but directionally insensitive. Therefore, a microstructure that combines lamellar and equiaxed regions (model 2) can result in improved fracture resistance as equiaxed regions can effectively deflect cracks away from the weak orientation of their neighboring lamellar regions. As a result, we observed that the dislocation density and the magnitude of damage near the crack-tip in model 2 were significantly lower than in model 1-h and model 3, but close to that in model 1-v (inset of Fig. 6d and Fig. 6i).

These findings of delocalized damages are consistent with our experimental observations of distributed micro-cracking in the proximity of the major crack (Fig. 3c and Supplementary Fig. 13). At a fundamental level, the phenomenon of transformation induced plasticity (TRIP) is closely linked to SFE. Therefore, similar phenomena have been reported for binary alloys<sup>63,64</sup>, highlighting the importance of SFE in TRIP. However, the SFE can be adjusted by altering the chemical composition of an alloy. HEAs offer a wide compositional space and their inherent compositional complexity allows for significant tunability of the SFE. Therefore, we believe that the compositional window for SFE tuning is broader in HEAs compared to binary alloys. Regarding the delocalization of microcracks, our results clearly demonstrate that it is a general toughening mechanism stemming from microstructural heterogeneities, which applies to both low-order systems (binary and ternary) and high-order systems like HEAs.



However, the fine-scale microstructural features, potentially resulting from sluggish atom diffusion in EHEAs<sup>65</sup>, provide us with a larger thermomechanical processing window for fine-tuning the microstructural heterogeneities, therefore facilitating the microstructural optimization for enhance toughness.”

## Conclusion

In summary, we have successfully engineered a high-strength, ductile EHEA by fine-tuning its chemical and microstructural heterogeneities through thermomechanical processing. The optimization of chemical heterogeneity at both atomic- and nano-scales resulted in dynamic strain hardening, triggered by deformation-induced FCC-BCC transition at the FCC/BCC interface with a K-S orientation relationship. Simultaneously, thermal annealing spurred microstructural evolution, transforming a typical lamellar to a near-equiaxed microstructure. This transition led to the coexistence of these two microstructures at the meso-scale, creating a hybrid microstructure. Interestingly, the combined microstructure effectively initiated distributed micro-cracking and bolstered the fracture resistance of the alloy, thereby enhancing its room-temperature ductility even under high flow stresses, a feat unattainable with either a lamellar or a near-equiaxed microstructure alone. We anticipate that our current findings could have broader applications for other eutectic structural alloys with significant technological value, such as those used in the automotive, aerospace, and nuclear industries<sup>3,18,66,67</sup>.

## Methods

**Materials preparation.** The EHEAs with the chemical composition of  $\text{Al}_{18}\text{Co}_{30}\text{Cr}_{11}\text{Fe}_{11}\text{Ni}_{30}$  were prepared by arc-melting with high-purity raw materials (>99.9 wt%) in a Ti-gettered argon atmosphere. Each ingot was melted at least five times to obtain the chemical homogeneity and then dropped into a water-cooled copper mold with a dimension of  $60 \times 12.5 \times 5 \text{ mm}^3$ . The as-cast alloy was cold-rolled to 70% reduction in thickness (labeled as AC and CR alloys) using a lab-scale two-high rolling machine and then annealed at 700 °C, 800 °C, 900 °C for 6 h followed by water quenching (labeled as P1, P2, P3 alloys).

**Microstructural characterization.** The crystalline phase was identified using X-ray diffraction (XRD) on a Rigaku MiniFlex 600 with Cu K $\alpha$  radiation and a scanning rate of 4° per min. Scanning electron microscopy (SEM) and EBSD were conducted in a FEI Quanta 450 FEG system with energy-dispersive spectroscopy detector and EDAX TSL system for microstructural and compositional analyses. The samples were initially polished using 2000-grit SiC abrasive papers and subsequently with Alumina suspension down to 0.3  $\mu\text{m}$ . The EBSD samples were further vibration polished in a BUEHLER Vibromet Polish machine with the colloidal silica suspension down to 0.02  $\mu\text{m}$ . The TEM and STEM-EDX analyses were conducted on a JEOL 2100F TEM. TEM samples were prepared by mechanically grinding to  $\sim 50 \mu\text{m}$  and subsequent ion-milling on a Gatan PIPS II System.

**Tensile test.** Room-temperature tensile tests were conducted on a MTI SEMtester1000 system with a strain rate of  $1 \times 10^{-3} \text{ s}^{-1}$ . The dog bone-shaped tensile samples with a cross-section of  $4.0 \times 0.5 \text{ mm}$  and a gauge length of 12 mm were cut by wire cutting. The tensile direction was parallel to the rolling direction. 3D X-ray CT scanning was performed on the NanoVoxel-3000 system with a spatial resolution of 10  $\mu\text{m}$  to characterize the number and morphology of pores in the as-cast sample to exclude their effects on mechanical properties. The tensile strain was obtained using the digital image correlation technique with the

open-source Ncorr code<sup>68</sup> implemented in MATLAB software. To provide sufficient contrast, the speckle pattern was produced on the gauge region of tensile samples and tracked during the deformation. Each tensile test was repeated at least five times to ensure the data reproducibility.

**Molecular dynamics simulations.** Our MD simulations were performed at a low temperature of 10 K using an embedded atom method potential using Large-scale Atomic/Molecular Massively Parallel Simulator (LAMMPS)<sup>69,70</sup>. The sample has sizes of  $15.1 \times 41 \times 10.4 \text{ nm}^3$  and contains a total of  $\sim 530,000$  atoms. The crystal orientations are  $1\bar{1}0$  along the x direction,  $[111]$  along the y direction,  $[112]$  along the z direction for the fcc phase;  $[111]$  along the x direction,  $[110]$  along the y direction,  $[\bar{1}12]$  along the z direction for the bcc phase. Thus, the fcc/bcc interface meets the Kurdjumov-Sachs (K-S) lattice orientation relation. The periodic boundary conditions are imposed in the x, y, and z directions to eliminate the influence of the boundary effect. A shear load is applied in the xy direction at a constant strain rate of  $1 \times 10^8/\text{s}$ . The local structure is identified by the common-neighbor analysis using the visualization tool OVITO during the simulations<sup>71,72</sup>.

**Finite element simulations.** Finite element simulations were performed using an open-sourced finite element code, FEniCS<sup>73,74</sup>. Two-dimensional pre-cracked models ( $100 \times 100 \mu\text{m}^2$ ) were used with the mesh size of 1  $\mu\text{m}$ . Dual-phase polycrystalline microstructures were created by two-step numerical simulations of solidification using Cahn-Hilliard model<sup>61</sup> and Kobayashi-Warren-Carter model<sup>62</sup>. To simulate the elastoplastic deformation and damage behavior of the EHEA, we used a finite-strain dislocation-based crystal plasticity model<sup>59</sup> coupled with a phase-field fracture model<sup>60</sup>.

## Data availability

The data that support the findings of this study are available from the corresponding author upon reasonable request.

Received: 14 September 2023; Accepted: 21 January 2024;

Published online: 03 February 2024

## References

1. Buchanan, E. R. & Tarshis, L. A. Strengths and failure mechanisms of a Co-15Cr-13TaC directionally solidified eutectic alloy. *Metall. Mater. Trans. B* **5**, 1413–1422 (1974).
2. Zhang, G. S., Jing, H. Y., Xu, L. Y., Wei, J. & Han, Y. D. Creep behavior of eutectic 80Au/20Sn solder alloy. *J. Alloys Compd.* **476**, 138–141 (2009).
3. Chanda, B., Potnis, G., Jana, P. P. & Das, J. A review on nano-ultrafine advanced eutectic alloys. *J. Alloys Compd.* **827**, 154226 (2020).
4. Wu, W., Gong, M., Wei, B., Misra, A. & Wang, J. Atomistic modeling of interface strengthening in Al-Si eutectic alloys. *Acta Mater.* **225**, 117586 (2022).
5. Bei, H. & George, E. P. A Microstructures and mechanical properties of a directionally solidified NiAl-Mo eutectic alloy. *Acta Mater.* **53**, 69–77 (2005).
6. Jiang, L., Ruan, Y. & Wei, B. Microstructural evolution and mechanical properties of ternary Al-Fe-Nb alloy under free fall condition. *J. Alloys Compd.* **818**, 153304 (2020).
7. Liu, C. Y., Chen, C. & Tu, K. N. Electromigration in Sn-Pb solder strips as a function of alloy composition. *J. Appl. Phys.* **88**, 5703–5709 (2000).
8. Shalaby, R. M. Development of holmium doped eutectic Sn-Ag lead-free solder for electronic packaging. *Solder. Surf. Mt. Technol.* **5**, 277–286 (2022).
9. Yeh, J. W. et al. Nanostructured high-entropy alloys with multiple principal elements: Novel alloy design concepts and outcomes. *Adv. Eng. Mater.* **6**, 299–303 (2004).
10. Cantor, B., Chang, I. T. H., Knight, P. & Vincent, A. J. B. Microstructural development in equiatomic multicomponent alloys. *Mater. Sci. Eng. A* **375–377**, 213–218 (2004).

11. Lu, Y. et al. A promising new class of high-temperature alloys: eutectic high-entropy alloys. *Sci. Rep.* **4**, 6200 (2014).
12. Gao, X. et al. Microstructural origins of high strength and high ductility in an AlCoCrFeNi<sub>2.1</sub> eutectic high-entropy alloy. *Acta Mater.* **141**, 59–66 (2017).
13. Lu, Y. et al. Directly cast bulk eutectic and near-eutectic high entropy alloys with balanced strength and ductility in a wide temperature range. *Acta Mater.* **124**, 143–150 (2017).
14. Wang, Q., Lu, Y., Yu, Q. & Zhang, Z. The Exceptional Strong Face-centered Cubic Phase and Semi-coherent Phase Boundary in a Eutectic Dual-phase High Entropy Alloy AlCoCrFeNi. *Sci. Rep.* **8**, 14910 (2018).
15. Baker, I., Wu, M. & Wang, Z. Eutectic/eutectoid multi-principle component alloys: a review. *Mater. Charact.* **147**, 545–557 (2019).
16. Shi, P. et al. Enhanced strength–ductility synergy in ultrafine-grained eutectic high-entropy alloys by inheriting microstructural lamellae. *Nat. Commun.* **10**, 489 (2019).
17. Reddy, S. R. et al. Nanostructuring with structural-compositional dual heterogeneities enhances strength–ductility synergy in eutectic high entropy alloy. *Sci. Rep.* **9**, 11505 (2019).
18. Lu, Y. et al. Promising properties and future trend of eutectic high entropy alloys. *Scr. Mater.* **187**, 202–209 (2020).
19. Tiwary, C. S. et al. Five decades of research on the development of eutectic as engineering materials. *Prog. Mater. Sci.* **123**, 100793 (2022).
20. Chen, Z. & Yang, Y. Data-driven design of eutectic high entropy alloys. *J. Mater. Inform.* **3**, 11505 (2023).
21. Shi, P. et al. Hierarchical crack buffering triples ductility in eutectic herringbone high-entropy alloys. *Science*. **373**, 912–918 (2021).
22. Wani, I. S. et al. Ultrafine-grained AlCoCrFeNi<sub>2.1</sub> eutectic high-entropy alloy. *Mater. Res. Lett.* **4**, 174–179 (2016).
23. Shi, P. et al. Multistage work hardening assisted by multi-type twinning in ultrafine-grained heterostructural eutectic high-entropy alloys. *Mater. Today* **41**, 62–71 (2020).
24. Xiong, T., Zheng, S., Pang, J. & Ma, X. High-strength and high-ductility AlCoCrFeNi<sub>2.1</sub> eutectic high-entropy alloy achieved via precipitation strengthening in a heterogeneous structure. *Scr. Mater.* **186**, 336–340 (2020).
25. Guo, T. et al. Microstructure and properties of bulk Al<sub>0.5</sub>CoCrFeNi high-entropy alloy by cold rolling and subsequent annealing. *Mater. Sci. Eng. A* **729**, 141–148 (2018).
26. Wu, Q. et al. Phase-selective recrystallization makes eutectic high-entropy alloys ultra-ductile. *Nat. Commun.* **13**, 4697 (2022).
27. Jin, X., Zhou, Y., Zhang, L., Du, X. & Li, B. A new pseudo binary strategy to design eutectic high entropy alloys using mixing enthalpy and valence electron concentration. *Mater. Des.* **143**, 49–55 (2018).
28. Liu, W. H. et al. Effects of Nb additions on the microstructure and mechanical property of CoCrFeNi high-entropy alloys. *Intermetallics* **60**, 1–8 (2015).
29. Niu, S. et al. Strengthening of nanoprecipitations in an annealed Al<sub>0.5</sub>CoCrFeNi high entropy alloy. *Mater. Sci. Eng. A* **671**, 82–86 (2016).
30. Tian, Q. W. et al. Effect of Ni content on the phase formation, tensile properties and deformation mechanisms of the Ni-rich AlCoCrFeNi<sub>x</sub> (x = 2, 3, 4) high entropy alloys. *Mater. Charact.* **176**, 111148 (2021).
31. Liu, M. et al. Microstructures and hardnesses of AlCoCr<sub>0.5</sub>FeNi<sub>2.5</sub> high entropy alloys with equal valence electron concentration. *J. Alloys Compd.* **824**, 153881 (2020).
32. Feng, R. et al. Enhancing fatigue life by ductile-transformable multicomponent B2 precipitates in a high-entropy alloy. *Nat. Commun.* **12**, 1–10 (2021).
33. Kim, H. W., Kang, S. U. K. B. & Tsuji, N. Deformation textures of AA8011 aluminum alloy sheets severely deformed by accumulative roll bonding. *Metall. Mater. Trans. A* **36**, 3151–3163 (2005).
34. Sauvage, X., Enikeev, N., Valiev, R., Nasedkina, Y. & Murashkin, M. Atomic-scale analysis of the segregation and precipitation mechanisms in a severely deformed Al-Mg alloy. *Acta Mater.* **72**, 125–136 (2014).
35. Mu, P. et al. Influence of casting defects on the fatigue behavior of cast aluminum AS7G06-T6. *Int. J. Fatigue* **63**, 97–109 (2014).
36. Niklas, A. et al. Effect of microstructure and casting defects on the mechanical properties of secondary AlSi10MnMg(Fe) test parts manufactured by vacuum assisted high pressure die casting technology. *Mater. Today Proc.* **2**, 4931–4938 (2015).
37. Wani, I. S. et al. Tailoring nanostructures and mechanical properties of AlCoCrFeNi<sub>2.1</sub> eutectic high entropy alloy using thermo-mechanical processing. *Mater. Sci. Eng. A* **675**, 99–109 (2016).
38. Tripathy, B., Malladi, S. R. K. & Bhattacharjee, P. P. Development of ultrafine grained cobalt-free AlCrFeNi<sub>2</sub> high entropy alloy with superior mechanical properties by thermo-mechanical processing. *Mater. Sci. Eng. A* **831**, 142190 (2022).
39. Park, J. M. et al. Effect of annealing heat treatment on microstructural evolution and tensile behavior of Al<sub>0.5</sub>CoCrFeMnNi high-entropy alloy. *Mater. Sci. Eng. A* **728**, 251–258 (2018).
40. Liu, X. et al. Enhanced dynamic deformability and strengthening effect via twinning and microbanding in high density NiCoFeCrMoW high-entropy alloys. *J. Mater. Sci. Technol.* **127**, 164–176 (2022).
41. A. C. *Mémoire sur l'emploi du fer et de l'acier dans les constructions. Annales des Ponts et Chaussées* vol. Vol 9 (1885).
42. Basinski, Z. S., Szczerba, M. S. & Embury, J. D. Tensile instability in face-centred cubic materials. *Philos. Mag. A Phys. Condens. Matter, Struct. Defects Mech. Prop.* **76**, 743–752 (1997).
43. Li, Q. et al. Superior tensile properties of Al<sub>0.3</sub>CoCrFeNi high entropy alloys with B2 precipitated phases at room and cryogenic temperatures. *Mater. Sci. Eng. A* **767**, 138424 (2019).
44. Jiang, L. et al. Tunable mechanical property and strain hardening behavior of a single-phase CoFeNi<sub>2</sub>V<sub>0.5</sub>Mo<sub>0.2</sub> high entropy alloy. *Mater. Sci. Eng. A* **776**, 139027 (2020).
45. Yang, J. et al. Improving mechanical properties of (Co<sub>1.5</sub>FeNi)<sub>88.5</sub>Ti<sub>6</sub>Al<sub>4</sub>R<sub>1.5</sub> (R = Hf, W, Nb, Ta, Mo, V) multi-component high-entropy alloys via multi-stage strain hardening strengthening. *Mater. Des.* **222**, 111061 (2022).
46. Xin, H. et al. Effects of Cold Rolling and Annealing Treatment on Microstructure and Properties of CoFeNiMnV High-Entropy Alloys. *Adv. Eng. Mater.* **25**, 1–12 (2023).
47. Cao, T. et al. The influence of Al elements on the structure and the creep behavior of AlxCoCrFeNi high entropy alloys. *Mater. Lett.* **164**, 344–347 (2016).
48. He, Q. F. et al. A highly distorted ultraelastic chemically complex Elinvar alloy. *Nature* **602**, 251–257 (2022).
49. Wang, H. et al. Multifunctional high entropy alloy enabled by severe lattice distortion. *Adv. Mater.* **n/a**, 2305453 (2023).
50. Maresca, F. & Curtin, W. A. The austenite/lath martensite interface in steels: Structure, athermal motion, and in-situ transformation strain revealed by simulation and theory. *Acta Mater.* **134**, 302–323 (2017).
51. Wei, Z. Z., Ma, X., Ke, C. B. & Zhang, X. P. Distinct migration mechanisms of stepped FCC/BCC martensitic interfaces associated with typical orientation relationships: a molecular dynamics study. *J. Mater. Sci.* **57**, 19857–19871 (2022).
52. Stukowski, A. & Albe, K. Extracting dislocations and non-dislocation crystal defects from atomistic simulation data. *Model. Simul. Mater. Sci. Eng.* **18**, 85001 (2010).
53. Wasilewski, R. J. On the nature of the martensitic transformation. *Metall. Trans. A* **6**, 1405–1418 (1975).
54. Nandi, S. & Kumar, S. Atomistic structural transformation of iron single crystal under bi-axial stretching using classical molecular dynamics simulation. *Bull. Mater. Sci.* **45**, 252 (2022).
55. Tateyama, S., Shibuta, Y. & Suzuki, T. A molecular dynamics study of the fcc-bcc phase transformation kinetics of iron. *Scr. Mater.* **59**, 971–974 (2008).
56. Offerman, S. E. et al. Grain nucleation and growth during phase transformations. *Science* **298**, 1003–1005 (2002).
57. Bourgeois, L., Zhang, Y., Zhang, Z., Chen, Y. & Medhekar, N. V. Transforming solid-state precipitates via excess vacancies. *Nat. Commun.* **11**, 1248 (2020).
58. Li, J., Fang, Q., Liu, B. & Liu, Y. Transformation induced softening and plasticity in high entropy alloys. *Acta Mater.* **147**, 35–41 (2018).
59. Liu, C., Roters, F. & Raabe, D. Finite strain crystal plasticity-phase field modeling of twin, dislocation, and grain boundary interaction in hexagonal materials. *Acta Mater.* **242**, 118444 (2023).
60. Miede, C., Welschinger, F. & Hofacker, M. Thermodynamically consistent phase-field models of fracture Variational principles and multi-field FE implementations. *Int. J. Numer. Methods Eng.* **83**, 1273–1311 (2010).
61. Cahn, J. W. & Hilliard, J. E. Free energy of a nonuniform system. I. Interfacial free energy. *J. Chem. Phys.* **28**, 258–267 (1958).
62. Warren, J. A., Kobayashi, R., Lobkovsky, A. E. & Carter, W. C. Extending phase field models of solidification to polycrystalline materials. *Acta Mater.* **51**, 6035–6058 (2003).
63. Yamagishi, K., Ogawa, Y., Ando, D. & Sutou, Y. Adjustable room temperature deformation behavior of Mg–Sc alloy: from superelasticity to slip deformation via TRIP effect. *J. Alloys Compd.* **931**, 167507 (2023).
64. Qian, B. et al. Mechanisms underlying enhanced strength–ductility combinations in TRIP/TWIP Ti–12Mo alloy engineered via isothermal omega precipitation. *Acta Mater.* **245**, 118619 (2023).
65. Tsai, K. Y., Tsai, M. H. & Yeh, J. W. Sluggish diffusion in Co–Cr–Fe–Mn–Ni high-entropy alloys. *Acta Mater.* **61**, 4887–4897 (2013).
66. Taub, A. I. Automotive materials: technology trends and challenges in the 21st century. *MRS Bull* **31**, 336–343 (2006).
67. Kumar Krovvidi, S. C. S. P., Padmakumar, G. & Bhaduri, A. K. Experience of various materials for design and manufacture of bellows for nuclear industry. *Adv. Mater. Proc.* **2**, 156–161 (2017).
68. Blaber, J., Adair, B. & Antoniou, A. Ncorr: open-source 2D digital image correlation matlab software. *Exp. Mech.* **55**, 1105–1122 (2015).
69. Plimpton, S. Fast parallel algorithms for short-range molecular dynamics. *J. Comput. Phys.* **117**, 1–19 (1995).
70. Zhou, X. W., Johnson, R. A. & Wadley, H. N. G. Misfit-energy-increasing dislocations in vapor-deposited CoFe/NiFe multilayers. *Phys. Rev. B - Condens. Matter Mater. Phys.* **69**, 1–10 (2004).

71. Faken, D. & Jónsson, H. Systematic analysis of local atomic structure combined with 3D computer graphics. *Comput. Mater. Sci.* **2**, 279–286 (1994).
72. Stukowski, A. Visualization and analysis of atomistic simulation data with OVITO—the Open Visualization Tool. *Model. Simul. Mater. Sci. Eng.* **18**, 015012 (2010).
73. Logg, A., Mardal, K. A. & Wells, G. N. *Automated Solution of Differential Equations by the Finite Element Method. Lecture Notes in Computational Science and Engineering*, Vol. 84 LNCSE (Springer Science & Business Media, 2012).
74. Alnaes, M. S. et al. The FEniCS project version 1.5. *Arch. Numer. Softw.* **3**, 9–23 (2015).

### Acknowledgements

Y.Y. acknowledges the financial support provided by the Research Grants Council, the Hong Kong Government, through the General Research Fund with the grant numbers (CityU 11201721, CityU11206362).

### Author contributions

Z.Q.C. and Y.Y. designed the research. Z.Q.C. prepared the samples and performed mechanical tests. X.D.L. conducted the XRD characterization. Z.Q.C. and H.W. conducted the EBSD characterization. Z.Q.C. and Q.F.H. conducted the TEM characterization. Q.H.F. and J.L. performed the MD simulation and analyzed the results. W.Q.Z. performed the FE simulations. Z.Q.C., W.Q.Z., and Y.Y. wrote the paper. Y.Y. supervised the research. All authors reviewed and commented on the manuscript.

### Competing interests

The authors declare no competing interests.

### Additional information

**Supplementary information** The online version contains supplementary material available at <https://doi.org/10.1038/s43246-024-00450-2>.

**Correspondence** and requests for materials should be addressed to Jia Li or Yong Yang.

**Peer review information** *Communications Materials* thanks the anonymous reviewers for their contribution to the peer review of this work. Primary Handling Editors: Eun Soo Park and John Plummer. A peer review file is available.

**Reprints and permission information** is available at <http://www.nature.com/reprints>

**Publisher's note** Springer Nature remains neutral with regard to jurisdictional claims in published maps and institutional affiliations.



**Open Access** This article is licensed under a Creative Commons Attribution 4.0 International License, which permits use, sharing, adaptation, distribution and reproduction in any medium or format, as long as you give appropriate credit to the original author(s) and the source, provide a link to the Creative Commons license, and indicate if changes were made. The images or other third party material in this article are included in the article's Creative Commons license, unless indicated otherwise in a credit line to the material. If material is not included in the article's Creative Commons license and your intended use is not permitted by statutory regulation or exceeds the permitted use, you will need to obtain permission directly from the copyright holder. To view a copy of this license, visit <http://creativecommons.org/licenses/by/4.0/>.

© The Author(s) 2024